Fe-Doped ZnO/Reduced Graphene Oxide Nanocomposite with Synergic Enhanced Gas Sensing Performance for the Effective Detection of Formaldehyde

ACS OMEGA

Article

Cite This: ACS Omega 2019, 4, 10252−10262

http://pubs.acs.org/journal/acsodf

Fe-Doped ZnO/Reduced Graphene Oxide Nanocomposite with Synergic Enhanced Gas Sensing Performance for the Effective Detection of Formaldehyde

Weiwei Guo,*[,†] Bangyu Zhao,[†] Qilin Zhou,[†] Youzhou He,[†] Zhongchang Wang,[‡] and Norbert Radacsi[§]

[†]Chongqing Key Laboratory of Catalysis and New Environmental Materials, College of Environment and Resources, Chongqing Technology and Business University, Chongqing 400067, People's Republic of China

[‡]Department of Quantum and Energy Materials, International Iberian Nanotechnology Laboratory (INL), Avenida Mestre Jose Veiga, Braga 4715-330, Portugal

[§]School of Engineering, Institute for Materials and Processes, The University of Edinburgh, King's Buildings, Edinburgh EH9 3FB, United Kingdom

Supporting Information

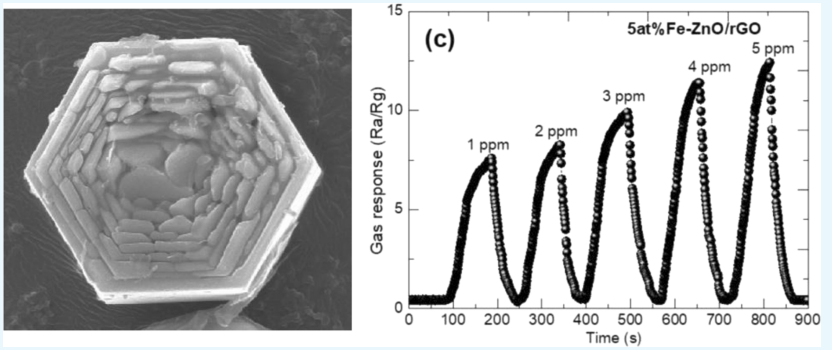

ABSTRACT: Here, we report the synthesis of Fe-doped ZnO/reduced graphene oxide (rGO) nanocomposites for gas sensing applications via a one-pot hydrothermal process. A wide range of characterization techniques were used to confirm the successful fabrication of the nanocomposite material and to determine the surface area, the structural and morphological properties, the chemical composition, and the purity of the samples, such as Brunauer−Emmett−Teller, X-ray diffraction, Fourier transform infrared, Raman spectroscopy, scanning electron microscopy, transmission electron microscopy, UV−vis spectroscopy, and X-ray photoelectron spectroscopy techniques. The gas sensing performance to formaldehyde was studied thoroughly in a temperature-controlled test chamber. Compared to that of the bare ZnO and ZnO/rGO nanocomposites, the as-prepared 5 atom % Fe-doped ZnO/rGO nanocomposites presented significantly enhanced gas sensing performance to formaldehyde at relatively low temperatures. Whereas most formaldehyde sensors operate at 150 °C and can detect as low as 100 ppm concentrations, the presented sensor can detect 5 ppm formaldehyde at 120 °C. Its fast response−recovery time, high stability, and high selectivity make it an ideal sensor; however, it can exhibit degenerative gas sensing performance at elevated relative humidity. The enhanced gas sensing mechanism was explained as the synergic effect of rGO and Fe doping. The results demonstrate that Fe doping and decorating the nanocomposite with rGO are promising approaches for achieving a superior gas sensing performance for the development of ZnO gas sensors for the detection of formaldehyde.

1. INTRODUCTION

Formaldehyde (chemical formula: HCHO) is a naturally occurring gas, which is frequently encountered in everyday life and has a potential hazard to human health.[1] The World Health Organization (WHO) pointed out that a long-term exposure to formaldehyde even in low concentration can cause leukemia and cancer of blood-forming organs and young children are especially sensitive to it.[2] Hence, the trace detection of formaldehyde is vital for healthcare and environmental protection and the development of highly sensitive, low-power sensors with good formaldehyde selectivity is sorely needed.

Metal oxide-based chemical sensors (MOSs), such as SnO_2,[3] WO_3,[4] In_2O_3,[5] ZnO,[6] and Cu_2O[7] have been proposed as promising candidates for the detection of toxic pollutant gases. Among them, ZnO is an interesting material due to its

Received: March 16, 2019
Accepted: May 31, 2019
Published: June 13, 2019

DOI: 10.1021/acsomega.9b00734
ACS Omega 2019, 4, 10252−10262

excellent chemical stability and electronic structure[8] and has good sensitivity to formaldehyde at elevated temperatures.[9] However, the formaldehyde gas sensing properties of pure ZnO are poor around room temperature.[10] Formaldehyde detection at low working temperatures would be desirable for its efficient real-time detection.

Recently, owing to the large specific surface area and superb electronic properties, reduced graphene oxide (rGO) is used as the modification material for sensing applications.[11] So far, many rGO-based gas sensors have been reported for the efficient detection of various volatile organic compounds.[12] For example, Lee et al. synthesized ZnO−rGO composites by a thermal annealing process and the gas sensitivity of the ZnO−rGO gas sensors to NO_2 was as high as 47.4% when the ZnO/rGO mass ratio was 0.08. The improved gas sensing mechanisms were attributed to the removal of oxygen-containing functional groups, the supply of electrons from the oxygen vacancies of ZnO material, and the formation of C−O−Zn bonds.[13] Rong et al. prepared a series of SnO_2/rGO nanocomposites with various rGO mass fractions and found that the sample with 0.5% rGO mass fraction had the highest response to HCHO vapors between 100 and 160 °C.[14] The enhanced formaldehyde-sensing performance is attributed to the high surface area of the nanocomposite and the suitable electron transfer channels of the rGO. Pan et al. synthesized rGO−Cu_2O nanocomposites by a facile solution-based self-assembly method.[15] The rGO/Cu_2O composite with 1 wt % rGO exhibited excellent selectivity, rapid response and recovery time, and 2.8 times higher response than that of the pristine Cu_2O, all of this at room temperature. The enhanced sensing behavior was attributed to the incorporation of rGO, which increased the gas adsorption active sites and allowed the fast transport of carriers. Thus, decorating MOSs with rGO seems to be an effective method for enhancing gas sensing properties.

To further improve the sensing performance of the rGO−MOS, chemical doping or compositing with a third phase was also carried out by many researchers. For instance, Bhati et al. synthesized Ni-doped ZnO sensors decorated with 0.75 wt % rGO by the radio frequency sputtering method. The sensor showed the maximum sensing response of ∼63.8% for 100 ppm hydrogen at 150 °C, and the sensor was able to detect hydrogen concentrations as low as 1 ppm.[16] Esfandiar et al. fabricated hydrogen sensors based on Pd−WO_3−rGO sheets that were fabricated by a hydrothermal process, and the sensor was sensitive to 20 ppm concentration of H_2 gas even at room temperature. The enhanced gas sensing performance was attributed to the effect of residual oxygen-containing functional groups of rGO and the morphology of metal oxide/graphene-based hybrid nanostructures.[17] Wang et al. reported SnO_2 nanoparticle-embedded, nitrogen-doped rGO (SnO_2/N-rGO) hybrids by a hydrothermal method, and the incorporation of N atoms into the SnO_2/rGO hybrids significantly enhanced the NO_2 sensing performance at room temperature, in comparison to SnO_2/rGO hybrids.[18] Although rGO−MOS nanocomposites for the application as gas sensors are numerous, additional doping of this nanocomposite to further improve the gas sensing performance is rarely reported.

In the natural world, Fe is one of the most common elements. Fe ion radius and valence are different from those of Zn ion; when Fe is doped into the ZnO matrix, the lattice distortion happens easily and also a large number of crystal defects are produced;[19] hence, Fe is chosen as the doping element in this study.

Herein, we report a one-pot hydrothermal process to prepare the Fe-doped ZnO/rGO nanocomposites. According to the structural and morphological characterizations, Fe-doped ZnO/rGO nanocomposites were successfully prepared. Compared to those of the pristine ZnO and ZnO/rGO nanocomposites, the 5 atom % Fe-doped ZnO/rGO nanocomposites presented a largely enhanced gas response and a fast response and recovery rate toward formaldehyde at low temperature below 150 °C, implying that the Fe-doped ZnO/rGO nanocomposites could be used for low-temperature gas sensing applications. Based on the above results, the gas sensing mechanism was also discussed in detail. The enhanced gas sensing performance of the Fe-doped ZnO/rGO nanocomposites could be attributed to the large specific surface area, the formation of p−n heterojunction, and more oxygen vacancies.

2. EXPERIMENTAL DETAILS

2.1. Preparation of Sensing Materials. The graphene oxide (GO) synthesis procedure was the following: 1 g of graphite powder and 3 g of $KMnO_4$ were added into 25 mL of concentrated H_2SO_4 in a flask under vigorous stirring at 0 °C. Next, 50 mL of distilled water was mixed into the suspension and the temperature was increased to 100 °C, where it was kept for 60 min. The reaction was stopped by adding 100 mL of distilled water and 10 mL of 30% H_2O_2 solution. Finally, the products were filtrated and washed with 5% HCl, then with ethanol for 5 times, and dried in vacuum at 60 °C for 12 h.

The 5 atom % Fe-doped ZnO/rGO nanocomposites (simply expressed as 5 atom % Fe−ZnO/rGO) were prepared via a hydrothermal method. First, 0.02 g of GO was dispersed into 20 mL of ethanol and sonicated for 2 h in an ultrasonic bath to obtain uniform GO dispersion. Zinc acetate (2 mM), ferric trichloride (0.1 mM), and poly(vinyl pyrrolidone) (0.2 g) were dissolved in distilled water (20 mL) under magnetic stirring to form a homogeneous white milky solution. Then, the GO solution was introduced into the above solution and stirred for 60 min to form a uniform mixture, transferred into a 50 mL autoclave, and heated at 160 °C for 12 h. Finally, the precipitates were washed and dried in air at 60 °C for 10 h. Meanwhile, 2.5 atom % Fe−ZnO/rGO, 7.5 atom % Fe−ZnO/rGO, ZnO/rGO, and pure ZnO samples were also synthesized using the identical procedure with adding different Ferric trichloride ratios or GO for comparison.

2.2. Characterization of the Materials. A Rigaku D/Max-1200X diffractometer with Cu Kα radiation was applied for X-ray diffraction (XRD) analysis. Fourier transform infrared (FTIR) spectra were recorded on a Nicolet Nexus spectrometer. The Raman spectra were measured by a Renishaw In Via spectrometer at 532 nm wavelength. Hitachi S-4300 SEM and JEOL TEM-2010F were used to observe the surface morphology of the samples. The specific surface area was measured on a surface area analyzer (Micromeritics, ASAP 2020M) using the Brunauer−Emmett−Teller (BET) model. The UV−vis spectra were obtained by a UV−vis spectrophotometer (UV-2450, Shimadzu, Japan). The X-ray photoelectron spectroscopy (XPS) was operated by using an Al Kα X-ray ($h\nu$ = 1486.6 eV) radiation source (Thermo ESCALAB 250) to investigate the surface chemical compositions and states. The electron paramagnetic resonance (EPR)

DOI: 10.1021/acsomega.9b00734
ACS Omega 2019, 4, 10252−10262

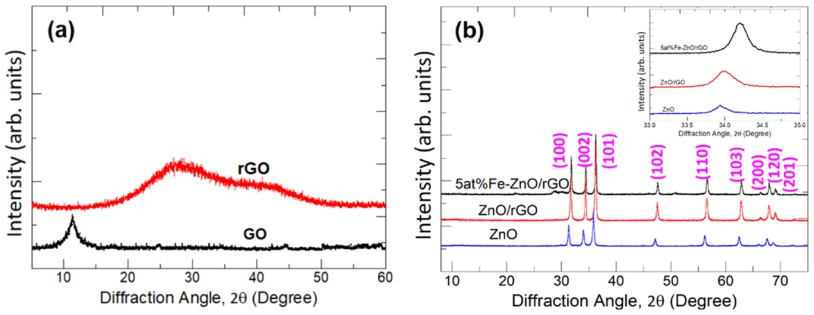

Figure 1. (a) XRD spectra of GO and rGO samples. (b) XRD spectra of ZnO, ZnO/rGO, and 5 atom % Fe−ZnO/rGO samples; the inset show the (002) diffraction peaks of ZnO, ZnO/rGO, and 5 atom % Fe−ZnO/rGO samples.

spectra were recorded at 25 °C on a Bruker ER-200D EPR spectrometer.

2.3. Gas Sensor Fabrication and Measurement. The gas sensing performance of the sample was tested by a CGS-1TP gas sensor testing system (Beijing Elite Tech. Co. Ltd). The Al_2O_3 substrate (8 × 15 × 1.5 mm^3) with Ag−Pd interdigitated electrodes was used to prepare the film sensor (Figure S1a). First, the as-synthesized products were ground and mixed with distilled water, then pasted onto the Ag−Pd interdigitated electrodes to form a thick sensing film of ∼1 mm, and dried at 60 °C for 5 h to ensure that the sensing film was smooth and free of bubbles and cracks (Figure S1b). The operating temperature was controlled by the heating system, and the relative humidity (RH) was set based on the needs of the experiment. The target gas was filled into the test chamber through the injection pore, and the fans for gas diffusion were turned on. When the gas response reached a constant value, the test chamber was purged with the fresh air and the fans were turned off. The filling and purging times of the test chamber were about 1 and 2 s, respectively, which were not calculated in the response and recovery times. Here, the gas response is defined as $S = R_a/R_g$, and the response and recovery times are defined as the total resistance change time (from 0 to 90 %) of the sensor on contact with the target gas and fresh air. The detailed operation procedures of the gas sensing testing process are described elsewhere.[20]

3. RESULTS AND DISCUSSION

3.1. Characterizations of the Sensing Materials. The XRD patterns of GO, rGO, ZnO, ZnO/rGO, and 5 atom % Fe−ZnO/rGO samples are displayed in Figure 1. As shown in Figure 1a, the XRD spectra of GO show a distinct diffraction peak at 2θ of around 11.6°, which is the typical peak for GO,[21] indicating the successful oxidation of graphite powders. After reduced in the hydrothermal process for GO, the diffraction peak between 24 and 30° is attributed to the (002) plane of rGO.[21] In Figure 1b, the diffraction peaks of ZnO, ZnO/rGO, and 5 atom % Fe−ZnO/rGO samples are all corresponding to the (101), (002), (101), (102), (110), (103), (200), (120), and (201) diffractions of ZnO ($P6_3mc$, JCPDS 36-1451), but all of the characteristic peaks of GO and rGO disappeared in the ZnO/rGO and 5 atom % Fe−ZnO/rGO samples. Based on the above results, no obvious rGO diffraction peaks appear in the XRD patterns of ZnO/rGO and 5 atom % Fe−ZnO/rGO samples, which may probably be ascribed to the small content of rGO. In addition, from the inset of Figure 1b, the position of the (002) diffraction peak of 5 atom % Fe−ZnO/rGO is shifted slightly to high diffraction angle compared to that of pure ZnO and ZnO/rGO, which reveals the change in lattice parameters. The change in lattice parameters can be attributed to the ionic radius of Zn^{2+} (0.74 Å), which is significantly larger than the ionic radius of Fe^{3+} (0.645 Å). Based on the Scherrer equation, the crystallite sizes of ZnO, ZnO/rGO, and 5 atom % Fe−ZnO/rGO are calculated to be 51.9, 50.1, and 39.9 nm, respectively. The results indicated that adding rGO did not change the crystallite sizes of ZnO and that rGO nanosheets were simply absorbed on the surface of the ZnO. Base on the above XRD results, Fe^{3+} ions were successfully incorporated into the ZnO lattice and reduced the crystallite sizes of ZnO.

Figure 2 presents the Raman spectra of GO, rGO, ZnO/rGO, and 5 atom % Fe−ZnO/rGO samples. All of the samples

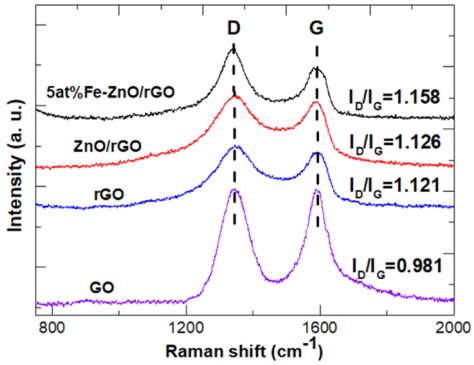

Figure 2. Raman spectra of GO, rGO, ZnO/rGO, and 5 atom % Fe−ZnO/rGO samples.

show the strong characteristic peaks located at 1350 and 1582 cm^{-1} corresponding to D and G bands, which are the typical graphene characteristic peaks.[22] The intensity ratios of D to G bands (I_D/I_G) of the rGO, ZnO/rGO, 5 atom % Fe−ZnO/rGO nanocomposites are 1.121, 1.126, 1.158, respectively, higher than that of GO (0.981), which can be attributed to the partial modification of surface oxygen-containing functional groups. The Raman results indicated that the reduction of GO was successful after the hydrothermal treatment.[23]

The FTIR spectroscopy is used to analyze the chemical bond structures of the GO, ZnO/rGO, and 5 atom % Fe−ZnO/rGO samples. In Figure S2, the FTIR spectrum of GO illustrates several distinct strong peaks related to oxygen functional groups at 1242 cm^{-1} (C−OH), 1618 cm^{-1} (C−O−C), 1752 cm^{-1} (C═O), and 3455 cm^{-1} (OH).[24] However, after hydrothermal treatment, all of the adsorption peaks of oxygen functional groups in ZnO/rGO and 5 atom % Fe−ZnO/rGO samples become weaker or even disappear, which indicates that the rGO can be successfully produced by the

DOI: 10.1021/acsomega.9b00734
ACS Omega 2019, 4, 10252−10262

hydrothermal method. Notably, the new peaks of the Zn−O bond appear in only ZnO/rGO and 5 atom % Fe−ZnO/rGO at around 518−632 cm^{-1}; the Zn−O symmetrical stretching vibration indicates the dispersion of ZnO on the rGO nanosheets.[25] However, the C═C adsorption peaks in ZnO/rGO and 5 atom % Fe−ZnO/rGO samples get a blueshift, which ascribes to the ZnO interacting with the rGO plane.[26]

Figure S3a shows the XPS spectra of 5 atom % Fe−ZnO/rGO products, which clearly confirms the existence of Fe, Zn, O, and C elements in the products. Figure S3b shows that the Fe 2p signal; the Fe $2p_{1/2}$ and Fe $2p_{3/2}$ peaks are located at 710.2 and 724.1 eV, respectively. However, a weak peak is located at 717.7 eV corresponding to γ-Fe_2O_3,[27] which indicates that Fe^{3+} is successfully incorporated into the ZnO lattice. In Figure S3c, the complex C 1s XPS spectra can be divided into four oxygen-containing functional groups peaks, corresponding to O−C═C, C−O−C/C═O, C−O, and C−C/C═C groups of rGO, which are located at 289.1, 286.3, 284.9, and 284.6 eV, respectively.[28] In Figure S3d, the Zn $2p_{3/2}$ and Zn $2p_{1/2}$ peaks are centered at 1044.8 and 1021.8 eV, respectively. From Figure S3e, the O 1s XPS peak is divided into three O_L (oxygen lattice), O_V (oxygen vacancy), O_C (chemisorbed oxygen) characteristic peaks by the Gaussian method, which are centered at 531.6, 532.9, and 533.4 eV, respectively.[29]

Figure 3 presents the scanning electron microscopy (SEM) images for the ZnO, ZnO/rGO, and 5 atom % Fe−ZnO/rGO

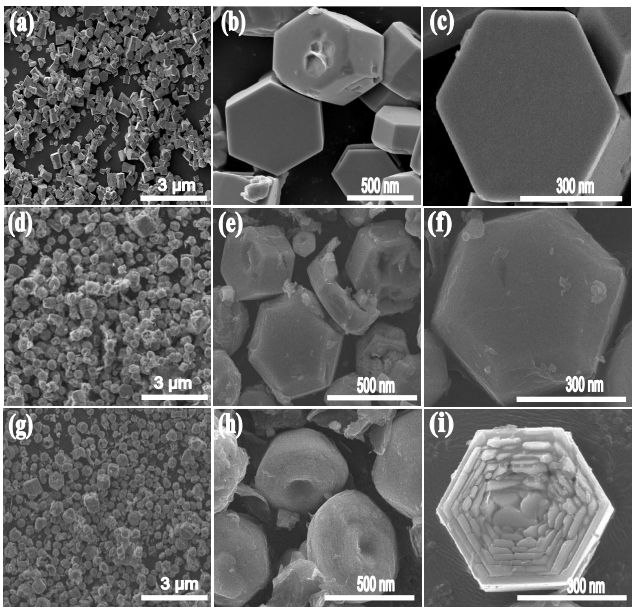

Figure 3. SEM and FESEM image of (a−c) ZnO samples, (d−f) ZnO/rGO samples, and (g−i) 5 atom % Fe−ZnO/rGO samples.

samples. Figure 3a−c depicts the SEM images of the pure ZnO at different magnifications. A large number of ZnO hexagonal prisms with good dispersity and uniform sizes can be observed in Figure 3a. The field-emission scanning electron microscopy (FESEM) images of Figure 3b,c, show that the hexagonal prism exhibits a smooth surface without any attachments. The SEM images of ZnO/rGO nanocomposites are shown in Figure 3d−f; the sizes of nanocomposites are not uniform as those of pure ZnO (Figure 3d), and the surface of the ZnO hexagonal prism becomes coarse and or even broken. Notably, from the FESEM images of Figure 3e,f, some thin rGO nanosheets covering the surface of ZnO hexagonal prisms can be observed. The SEM images of 5 atom % Fe−ZnO/rGO are displayed in Figure 3g−i, and it can be seen that the morphology and size of ZnO hexagonal prisms apparently change after doping with a certain amount of Fe, as the sides of the ZnO hexagonal prisms are fastigiate just like been intercepted (Figure 3g), and the subface of the ZnO hexagonal prism becomes coarse and loose. Moreover, from the FESEM images of Figure 3h,i, it is visible that some intervals and pores are also formed inside the ZnO hexagonal prisms and some thin rGO nanosheets are also attached on the surface of the ZnO hexagonal prisms. As a result, the size and morphology of the ZnO hexagonal prisms are changed by adding rGO and doping with Fe.

Figure S4a−e shows the results of the element mapping for the 5 atom % Fe−ZnO/rGO hexagonal prisms, confirming the presence of C, Fe, O, Zn elements. It can be seen that the Fe elements distribute uniformly in the ZnO hexagonal prisms and the C elements are mainly distributed around the ZnO hexagonal prisms, which are consistent with the XPS and SEM results. Figure S4h exhibits the transmission electron microscopy (TEM) images of the 5 atom % Fe−ZnO/rGO nanocomposites, and the rGO nanosheets attached on the surface of the ZnO hexagonal prisms can be clearly identified. The TEM image of partial rGO nanosheet is almost transparent, indicating that the rGO nanosheet is very thin. The SAED pattern of the 5 atom % Fe−ZnO/rGO nanocomposite is shown in the inset of Figure S4h, which reveals the polycrystalline structure of the as-prepared 5 atom % Fe−ZnO/rGO nanocomposite.

Figure S5 shows the BET surface area results and the pore distribution of the 5 atom % Fe−ZnO/rGO sample. The type IV physisorption isotherms and type H3 hysteresis loops reflect the existence of mesopores and slitlike pores in the 5 atom % Fe−ZnO/rGO sample (Figure S5a).[30] Moreover, Figure S5b shows that the pore size distributes from 5 to 80 nm and some open mesopores (~10.9 nm) indwell in the 5 atom % Fe−ZnO/rGO sample. The BET surface area and pore volume data of ZnO, ZnO/rGO, and 5 atom % Fe−ZnO/rGO are (16.5 m^2/g, 0.039 cm^3/g), (35.9 m^2/g, 0.055 cm^3/g), and (48.2 m^2/g, 0.061 cm^3/g), respectively. The 5 atom % Fe−ZnO/rGO sample exhibits the largest BET and pore volume. As far as we know, ZnO is a surface-controlled-type sensing material, so the increased BET and pore size can provide highly increased gas sensing reaction sites for the target gas molecules, resulting in the largely improved gas sensing performance.

3.2. Gas Sensing Properties. The optimum working temperature is of great importance for the gas sensor. Therefore, the gas response of the sensors based on ZnO, ZnO/rGO, 2.5 atom % Fe−ZnO/rGO, 5 atom % Fe−ZnO/rGO, and 7.5 atom % Fe−ZnO/rGO samples to 5 ppm formaldehyde were measured as a function of working temperature. Figure 4 shows the gas response of the sensors to 5 ppm formaldehyde at a different temperature from 20 to 270 °C. Interestingly, all of the sensors exhibit the maximum gas response at the optimum working temperature. The tested maximum gas response and optimum working temperature were S_{max} = 3.6 at 220 °C (ZnO), S_{max} = 8.2 at 120 °C (ZnO/rGO), S_{max} = 10.3 at 120 °C (2.5 atom % Fe−ZnO/rGO), S_{max} = 12.7 at 120 °C (5 atom % Fe−ZnO/rGO), *and* S_{max} = 7.6 at 120 °C (7.5 atom % Fe−ZnO/rGO), respectively. Notably, the sensor based on 5 atom % Fe−ZnO/rGO exhibits the

DOI: 10.1021/acsomega.9b00734
ACS Omega 2019, 4, 10252−10262

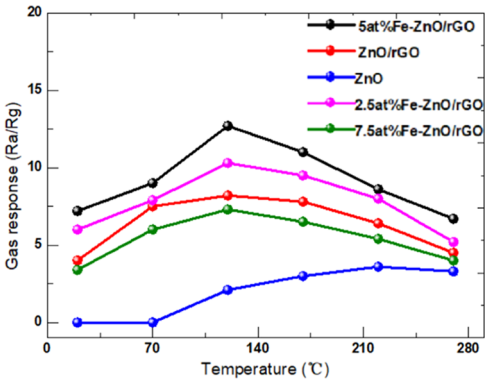

Figure 4. Gas responses of the sensors based on ZnO, ZnO/rGO, 2.5 atom % Fe−ZnO/rGO, 5 atom % Fe−ZnO/rGO, and 7.5 atom % Fe−ZnO/rGO samples vs operating temperatures to 5 ppm formaldehyde.

highest gas response to formaldehyde, which is almost 4 times higher than that of the pure ZnO. Meanwhile, the optimum working temperature of 5 atom % Fe−ZnO/rGO sensor has been dropped to about 100 °C compared to that of the pure ZnO sensor. On the other hand, the sensors based on the Fe-doped ZnO/rGO and ZnO/rGO exhibit a gas response signal even at room temperature (20 °C), but there is no gas response signal for the sensor based on pure ZnO at this temperature. From the above results, one can conclude that adding rGO can reduce the operating temperature and improve the gas response of ZnO. Moreover, doping Fe can further enhance the gas response for the ZnO/rGO composites and the optimum doping amount of Fe is 5 atom %. Therefore, the 5 atom % Fe−ZnO/rGO sample was chosen to investigate the gas sensing performance in details.

Since gas selectivity is a significant reference designator for the application of gas sensor, the gas responses of ZnO, ZnO/rGO, and 5 atom % Fe−ZnO/rGO sensors to 5 ppm to six typical indoor pollutant gases were measured at every sensor's optimum working temperature (220 °C for ZnO and 120 °C for ZnO/rGO and 5 atom % Fe−ZnO/rGO samples). Figure S6 shows the column diagram of the gas responses of three sensors to six typical indoor harmful volatile gases, including carbon monoxide (CO), benzene (C_6H_6), acetone (CH_3COCH_3), formaldehyde (HCHO), methylbenzene (C_7H_8), and ammonia (NH_3). From the column diagram, the ZnO, ZnO/rGO, and 5 atom % Fe−ZnO/rGO sensors all exhibit preferable selectivity toward formaldehyde. Notably, the 5 atom % Fe−ZnO/rGO sensor possesses the maximum gas response ratio value, where the gas response ratio is defined as $S_{\text{formaldehyde}}/S_{\text{other target gases}}$. The gas response ratio of the 5 atom % Fe−ZnO/rGO sensor is between 2.5 and 11.5, whereas the gas response ratio of the pure ZnO is only between 1.4 and 5.1. Usually, ammonia is considered as a much stronger reducing gas compared to formaldehyde,[31] but our sensor exhibits a higher gas response to formaldehyde than ammonia. As far as we know, in the gas sensing testing process, NH_3 may be more likely to bond with water molecules as $NH_3 \cdot H_2O$ and combines with ZnO to form $[Zn(H_2O)_m(NH_3)_n]^{2+}$ complexes further,[32] where m = 2, 3, 4, 6 and n = 0, 1, 2, 3, which consumed a mass of NH_3 and hindered the gas sensing reactions, resulting in the lower gas response of ammonia. Based on the above experimental results, the 5 atom % Fe−ZnO/rGO sensor exhibits good selectivity to formaldehyde.

Figure 5a−c shows the gas response of the ZnO, ZnO/rGO, and 5 atom % Fe−ZnO/rGO sensors to 1−5 ppm formaldehyde at their optimum working temperatures. The gas response curves of three sensors exhibit a continuing upward trend with the rise of formaldehyde concentration, but the gas

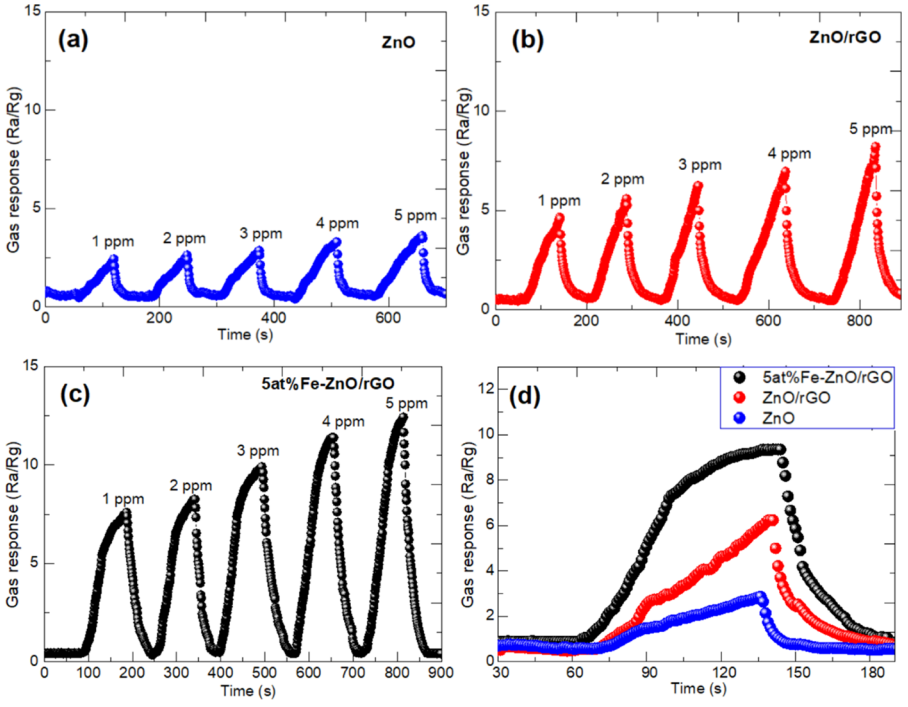

Figure 5. (a−c) Real-time response and recovery curves of the sensors based on ZnO, ZnO/rGO, and 5 atom % Fe−ZnO/rGO to 1−5 ppm formaldehyde at their optimum temperatures and (d) response and recovery times of the sensors based on ZnO, ZnO/rGO, and 5 atom % Fe−ZnO/rGO to 5 ppm formaldehyde at their optimum temperatures.

DOI: 10.1021/acsomega.9b00734
ACS Omega 2019, 4, 10252−10262

Table 1. Comparison of Formaldehyde Gas Sensing Performance between 5 atom % Fe−ZnO/rGO and Previously Reported ZnO- or rGO-Based Sensors

sensor materials	temperature (°C)	concentration (ppm)	gas response (R_a/R_g)	reference
5.5 wt % Fe-doped ZnO spheres	300	10	33	34
ZnO-doped In_2O_3	260	100	9	35
ZnO/Co_3O_4 hollow spheres	160	10	5.8	36
ZnO polyhedra	220	100	9.5	37
NiO/ZnO microflowers	200	100	26.2	38
graphene/ZnO nanosheets	200	100	12	39
rGO/flower-like ZnO	RT	10	6.5	40
GO-0.3%/SnO_2	150	200	90	41
In_2O_3@rGO heterostructures	225	100	2.5	42
rGO/$ZnSnO_3$ microspheres	103	10	12.8	43
5 atom % Fe−ZnO/rGO	120	5	12.7	This Work

response of 5 atom % Fe−ZnO/rGO is apparently higher than that of pure ZnO and ZnO/rGO to any one of the formaldehyde concentrations. Figure 5d displays the single response−recovery characteristic of the three sensors based on ZnO, ZnO/rGO, and 5 atom % Fe−ZnO/rGO to 5 ppm formaldehyde. The response and recovery times are evaluated to be 51 and 26 s for the ZnO sensor, 41 and 31 s for the ZnO/rGO sensor, and 34 and 37 s for 5 atom % Fe−ZnO/rGO sensor, respectively. Interestingly, the 5 atom % Fe−ZnO/rGO sensor exhibits a faster response time, but a longer recovery time than that of the other two sensors. The reason can be ascribed to the large specific surface area and plentiful pores of the 5 atom % Fe−ZnO/rGO sensor, which is beneficial for the gas diffusion and sensing reactions (e.g., high gas response and quick response time) but adverse to the gas desorption because of the long, flexible distribution of the cavities or pores in the materials (e.g., long recovery time).

The effect of the relative humidity on the behavior of the sensor based on 5 atom % Fe−ZnO/rGO to different formaldehyde concentrations was investigated with four different humidity conditions, dry, 20, 40, and 60% relative humidity (RH). As shown in Figure S7a−d, the gas response of the 5 atom % Fe−ZnO/rGO sensor decreased rapidly as the RH increased. On the other hand, the 5 atom % Fe−ZnO/rGO sensor exhibited a relatively stable and fast response−recovery time from the dry condition to 40% RH; however, at high humidity (60% RH), the response−recovery time became suddenly longer. In high RH conditions, the water vapor is absorbed on the rGO and ZnO surfaces, restricting the absorption of oxygen ions (O^- or O^{2-}) and blocking the surface to adsorb formaldehyde molecules. Therefore, the gas response of the Fe−ZnO/rGO sensor to formaldehyde was reduced and the response−recovery time was also prolonged. In general, the 5 atom % Fe−ZnO/rGO sensor exhibited the deteriorative gas sensing properties with the increasing humidity.

To meet the practical application for the detection of formaldehyde, the gas sensing properties of the sensor based on 5 atom % Fe−ZnO/rGO were tested comprehensively at 120 °C and 20% RH. Figure S8a shows the gas responses of the 5 atom % Fe−ZnO/rGO sensor to formaldehyde gas at different concentrations. The gas response value of our sensor exhibits a quickly increasing trend as the formaldehyde concentration achieves 45 ppm, then presents a period of slowly increasing trend as the formaldehyde concentration is further increasing, and finally reaches a saturation gas response value of ∼81.8 at 70 ppm formaldehyde concentration. Notably, the gas response of the 5 atom % Fe−ZnO/rGO sensor is increased almost linearly from 0.1 to 1 ppm formaldehyde concentration (see the inset of Figure S8a). The linear dynamic range is investigated from 0.1 to 1 ppm, which exhibits ∼4.667 about the slope ($\Delta_{(R_a/R_g)}/\Delta_{(\text{concentration})}$) of the linear curve. The theoretical limit of detection of the 5 atom % Fe−ZnO/rGO sensor to formaldehyde is calculated to be ∼19 ppb (signal-to-noise ratio > 3).[33]

The long-term stability of the 5 atom % Fe−ZnO/rGO sensor was also investigated, and the sensing measurements were tested at 1, 5, and 10 ppm formaldehyde for 6 weeks, as shown in Figure S8b. Throughout the three cyclic tests, the gas responses changed slightly 9.1, 8.3, and 7.1% to 1, 5, and 10 ppm formaldehyde gas, indicated that the 5 atom % Fe−ZnO/rGO sensor even had a good stability in low concentrations of formaldehyde, and the gas response of the 5 atom % Fe−ZnO/rGO sensor was more stable at high formaldehyde concentrations. In Table 1, the gas sensing performance to formaldehyde is compared between the fabricated 5 atom % Fe−ZnO/rGO sensor and the previously reported ZnO- or rGO-based sensors.[34−43] Our sensor presented excellent overall gas sensing properties (i.e., a working temperature at 120 °C and a gas response of 12.7) to 5 ppm formaldehyde, whereas most of the other formaldehyde sensors exhibited a working temperature above 150 °C and their gas responses were detected in formaldehyde concentrations above 100 ppm. Based on these results, the sensor based on 5 atom % Fe−ZnO/rGO should have the potential development and application for the trace detection of the formaldehyde gas.

3.4. Gas Sensing Mechanism. The separation efficiency of electron−hole can be analyzed by photoluminescence (PL) spectra. As shown in Figure S9a, PL spectra of the ZnO, ZnO/rGO, and 5 atom % Fe−ZnO/rGO samples exhibit similar emission peaks; the peaks at 397 and 423 nm for UV emission originate from the recombination of free excitons, and the enhanced peak at 476 nm for green emission is ascribed to the recombination of an electron to a photoexcited hole.[44] Figure S9b shows that the intensity of the green emission peak is significantly weakened as the rGO is added to the ZnO/rGO and 5 atom % Fe−ZnO/rGO samples, which is due to the excellent conductivity of rGO, similar to the Mott−Schottky effect.[45] Moreover, the rGO exhibits high carrier mobility and detectable resistance change for the adsorption or desorption of formaldehyde at room temperature due to superior electrical properties, which contribute to the lower working temperature of the ZnO/rGO composite than that of pure ZnO. This means adding rGO improved the electronic transfer efficiency

DOI: 10.1021/acsomega.9b00734
ACS Omega 2019, 4, 10252−10262

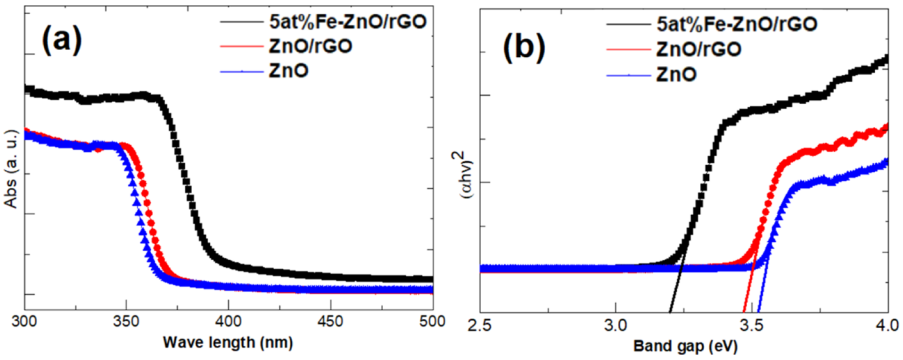

Figure 6. (a) UV−vis absorbance and reflectance spectra for ZnO, ZnO/rGO, and 5 atom % Fe−ZnO/rGO samples. (b) $(\alpha h\nu)^2$ versus $h\nu$ curves of the UV−vis spectra of ZnO, ZnO/rGO, and 5 atom % Fe−ZnO/rGO samples.

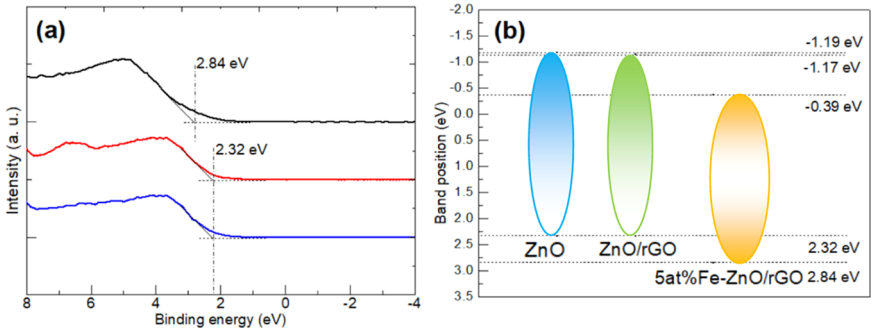

Figure 7. (a) Valence band (VB) XPS of ZnO, ZnO/rGO, and 5 atom % Fe−ZnO/rGO. (b) Energy band structures of ZnO, ZnO/rGO, and 5 atom % Fe−ZnO/rGO samples.

and conductivity of the ZnO/rGO nanocomposite, thereby further decreasing the working temperature, and enhanced the gas sensing performance of the ZnO-based gas sensor.

The band gaps of the ZnO, ZnO/rGO, and 5 atom % Fe−ZnO/rGO samples were studied by UV−vis spectroscopy. Figure 6a shows that all of the samples exhibit strong adsorption at ∼400 nm in the UV region. Notably, the 5 atom % Fe−ZnO/rGO sample exhibits an apparent redshift and extends its absorption area from UV to UV−vis, which means a new dopant energy level may be formed below the conduction band (CB) of ZnO. As far as we know, ZnO is a direct-band semiconductor; the relationship among the absorption coefficient (α), band gap (E_g), and photon energy ($h\nu$) is $\alpha h\nu = C(h\nu - E_g)^{1/2}$.[46] By extrapolating the ($h\nu$)−$(\alpha h\nu)^2$ plot to $(\alpha h\nu)^2 = 0$, Figure 6a can be transformed into Figure 6b. From Figure 6b, the E_g values for ZnO, ZnO/rGO, and 5 atom % Fe−ZnO/rGO are 3.51, 3.49, 3.23eV, respectively. It can be seen that rGO has almost no effect for the change of ZnO band gap, whereas Fe doping reduced the band gap of ZnO apparently.

In Figure 7a, the valence band (VB) levels of ZnO, ZnO/rGO, and 5 atom % Fe−ZnO/rGO are determined by VB XPS. The VB positions of ZnO, ZnO/rGO, and 5 atom % Fe−ZnO/rGO were 2.32, 2.32, and 2.84 eV, indicating that Fe doping resulted in the upshift for the VB position of ZnO. According to the band gap and VB position, we can calculate the conduction band (CB) positions of the ZnO, ZnO/rGO, and 5 atom % Fe−ZnO/rGO samples and the energy band diagram of the samples can be drawn. As shown in Figure 7b, adding rGO had no influence on the ZnO energy band structure, but doping with Fe adjusted the forbidden band position and moved up the CB and VB positions (the descending amplitude of CB was higher than that of VB). As a result, the band gap of ZnO was narrowed; therefore, the electrons can be released more easily from CB to VB in ZnO by thermal excitation.[47] The apparent upshift of the CB level was a benefit to generate more electrons, which would combine with surface-absorbed O_2 to form more absorbed oxygen ions (O_2^- and O_2^{2-}) and ultimately improved the gas sensing performance of the ZnO sensor by Fe doping.

Based on the XRD results, the doped Fe ions substituted for Zn ions in the ZnO matrix, whereas the appropriate oxygen vacancies ($V_O^{\bullet\bullet}$) would be produced due to different valences and ionic radii[48]

$$\mathrm{ZnO} \xrightarrow{\mathrm{Fe^{3+}}} \mathrm{Fe_{Zn}} + \frac{3}{2}\mathrm{O_O^{\times}} + \frac{1}{2}\mathrm{V_O^{\bullet\bullet}} \quad (1)$$

Here, Fe_{Zn} is the Fe substitution in Zn sites, $O_O^{\times}$ is the lattice oxygen, and $V_O^{\bullet\bullet}$ is the oxygen vacancy. Since the $V_O^{\bullet\bullet}$ center easily traps an electron to form a singly ionized $V_O^{\bullet}$, which causes EPR signal, EPR spectra can be used to evidence $V_O^{\bullet\bullet}$ in the samples.[49] As shown in Figure 8, a weak characteristic EPR signal of substitutional Fe^{3+} with a g value of 2.09 was detected for 5 atom % Fe−ZnO/rGO,[50] whereas no signal was observed for the ZnO and ZnO/rGO samples. On the other hand, ZnO, ZnO/rGO, and 5 atom % Fe−ZnO/rGO samples exhibited an EPR signal with a g value of 1.999, which rooted from the singly ionized oxygen vacancies ($V_O^{\bullet}$).[51] It can be seen from Figure 8 that ZnO and ZnO/rGO exhibited the same intensity of the EPR signal for $V_O^{\bullet}$; these oxygen vacancies were produced in the crystallization process of ZnO. Notably, 5 atom % Fe−ZnO/rGO exhibits the strongest EPR signal, which means that introducing Fe into ZnO nanocomposites significantly increased the number of oxygen vacancies. As far

DOI: 10.1021/acsomega.9b00734
ACS Omega 2019, 4, 10252−10262

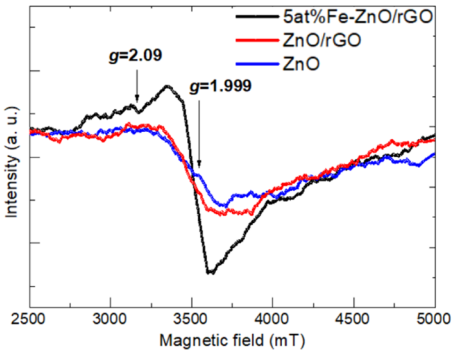

Figure 8. EPR spectra for ZnO, ZnO/rGO, and 5 atom % Fe−ZnO/rGO samples.

as we know, $V_O^{\bullet\bullet}$ often acts as an adsorption and a reaction site to form plentiful O_2^- and O_2^{2-}, respectively.[52] Hence, Fe doping provided a large number of gas adsorption sites and could trap electrons from ZnO easily, therefore increasing the electron depletion layer of the ZnO composites. The relative resistance change was dramatic when the 5 atom % Fe−ZnO/rGO sensor was exposed to air and formaldehyde, which enhanced the gas sensing performance remarkably.

The as-prepared 5 atom % Fe−ZnO/rGO nanocomposites consist of rGO nanosheets and Fe-doped ZnO spheres, where the rGO nanosheet is adsorbed tightly on the surface of the Fe-doped ZnO sphere (Figure 9a). When the ZnO sensor was exposed to air at a certain working temperature, the surface-absorbed oxygen ions (O^-, O^{2-}) were produced by trapping electrons from the CB of ZnO.

As the working temperature increased, more surface-absorbed oxygen ions were produced and an enlarged electron depletion layer was formed. This process reduced the carrier concentration, and the ZnO sensor material exhibited a high-resistance state, as shown in Figure 9b.

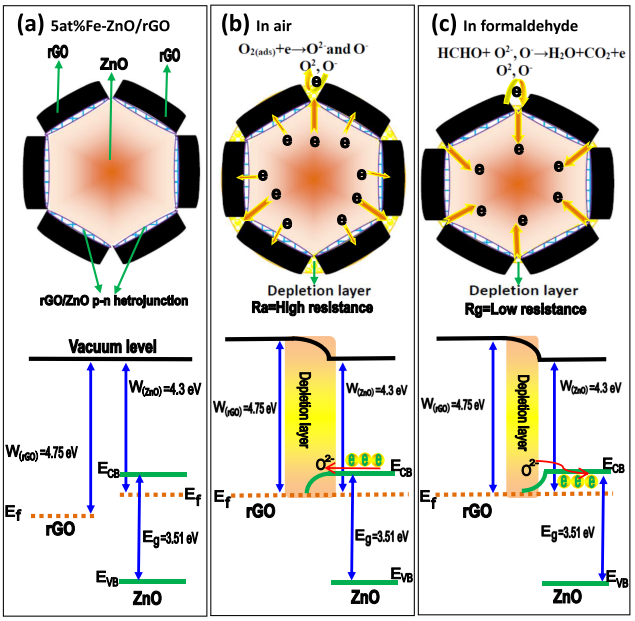

Figure 9. Schematic illustration of the formaldehyde gas sensing mechanism for 5 atom % Fe−ZnO/rGO nanocomposites. (a) Schematic of the 5 atom % Fe−ZnO/rGO nanocomposite. (b) Possible gas sensing reaction and electron transfer in air. (c) Possible gas sensing reaction and electron transfer in formaldehyde vapors.

When the ZnO sensor was exposed to formaldehyde, the formaldehyde gas molecules reacted with the adsorbed oxygen ions

$$HCHO_{(gas)} + O^-_{2(ads)} \rightarrow H_2O + CO_2 + e^- \quad (2)$$

$$HCHO_{(gas)} + 2O^-_{(ads)} \rightarrow H_2O + CO_2 + 2e^- \quad (3)$$

$$HCHO_{(gas)} + 2O^{2-}_{(ads)} \rightarrow H_2O + CO_2 + 4e^- \quad (4)$$

Therefore, the trapped electrons by the absorbed oxygen were released back into the CB of ZnO, which decreased the electron depletion layer, resulting in a low-resistance state, as shown in Figure 9c.

Figure S10 shows the resistance change curves of the sensors based on rGO and ZnO exposed in air and 5 ppm formaldehyde at 120 °C. It can be observed from Figure S10 that the rGO exhibits a typical p-type resistance curve, whereas the ZnO exhibits a typical n-type resistance curve. Bhati et al. also reported that rGO often exhibits the p-type semiconductor property with the work function of ∼4.75 eV and ZnO is an n-type semiconductor with the work function of ∼4.3 eV.[16] Based on the above results, the proposed enhanced gas sensing mechanism is shown in Figure 9. When ZnO/rGO composites were produced in the hydrothermal process, the p−n heterojunctions could be formed at the interface of ZnO/rGO composites (Figure 9a).[53,54] It is known that the majority charge carriers are holes in p-type rGO, whereas the majority charge carriers are electrons in n-type ZnO.[55,56] Due to the lower work function of ZnO and the superconductive property of rGO, the holes are transferred from rGO to ZnO and electron conduction will take place from n-ZnO to p-rGO at the interface between ZnO and rGO.[57] Hence, when the ZnO/rGO composites were heated to a certain temperature, the thermionic electrons in the CB of ZnO would transfer from ZnO to rGO in the p−n heterojunctions, which accelerated the carrier (electrons and holes) separation efficiency in ZnO. In another aspect, rGO often presents a zero band gap, like a metallic junction,[58] and the Fermi level of rGO is more positive than the CB position of ZnO, so the thermionic electrons transfer from ZnO to rGO is a low-energy consumption process, which would decrease the working temperature for the 5 atom % Fe−ZnO/rGO sensor. In the electron transfer process, a thick depletion layer was formed in p−n heterojunctions, which can be enlarged further as the working temperature kept going on; meanwhile, the resistance of the 5 atom % Fe−ZnO/rGO sensor increased drastically. After the electronic transmission achieved a dynamic balance, band bending occurred at the ZnO/rGO heterojunctions and the resistance of the 5 atom % Fe−ZnO/rGO sensor reached a maximum value (i.e., increasing the electron depletion layer) (Figure 9b). When the 5 atom % Fe−ZnO/rGO sensor was exposed to formaldehyde, the adsorbed oxygen ions reacted with formaldehyde and the trapped electrons flew back into the CB of ZnO, which decreased the electron depletion layer, and finally the 5 atom % Fe−ZnO/rGO sensor arrived at the lowest resistance value (Figure 9c). This gas sensing reaction process resulted in the sharp resistance change of the 5 atom % Fe−ZnO/rGO sensor, which improved the gas sensing performance to formaldehyde significantly. On the other hand, the Fe doping adjusted the forbidden band position and the band gap of ZnO was narrowed. Meanwhile, Fe doping

DOI: 10.1021/acsomega.9b00734
ACS Omega 2019, 4, 10252−10262

produced abundant oxygen vacancies in the ZnO host, which acted as gas adsorption or reaction sites to form plentiful absorbed oxygen ions (O_2^- and O_2^{2-}), and the gas sensing performance toward formaldehyde was further enhanced. Moreover, adding rGO and doping Fe also decreased the size of ZnO hexagonal prisms; therefore, the surface area and pore size of the 5 atom % Fe−ZnO/rGO nanocomposite were increased effectively, which provided much more gas sensing reaction sites for the target gas molecules, resulting in the largely improved gas sensing performance. Hence, doping Fe and decorating with rGO nanosheets have the synergistic effect to enhance the gas sensing properties of ZnO.

4. CONCLUSIONS

Fe-doped ZnO/rGO nanocomposites were successfully fabricated by a one-pot hydrothermal process. Adding rGO and doping with Fe decreased the size of ZnO hexagonal prisms and increased the surface area of the ZnO nanocomposites. Compared with the bare ZnO and ZnO/rGO, the 5 atom % Fe−ZnO/rGO nanocomposites presented a largely improved gas sensing performance at relatively low temperature toward formaldehyde. The sensor based on 5 atom % Fe−ZnO/rGO exhibits gas response of 12.7−5 ppm formaldehyde at 120 °C, response and recovery times as short as 34 and 37 s, respectively, and good stability and selectivity, but the sensor also shows degenerative gas sensing performance above 40% RH. Based on the gas sensing performance for the 5 atom % Fe−ZnO/rGO sensor, the gas sensing mechanism was also proposed in detail, the largely improved gas sensing properties could be attributed to the large specific surface area, the rGO-ZnO heterojunction, the narrowed band gap, and plentiful oxygen vacancies. It appears that the sensor based on 5 atom % Fe−ZnO/rGO has the potential development and application for the trace detection of the formaldehyde gas.

■ ASSOCIATED CONTENT

Supporting Information

The Supporting Information is available free of charge on the ACS Publications website at DOI: 10.1021/acsomega.9b00734.

FTIR spectra; XPS spectra; elements mapping and TEM images; specific surface area data; gas responses of the sensors; real-time response and recovery curves of the sensor at different RHs; gas response of the sensor to different formaldehyde concentrations and long-term gas response stability; PL spectra; and resistance change curves (PDF)

■ AUTHOR INFORMATION

Corresponding Author

*E-mail: gwctbu@163.com.

ORCID

Weiwei Guo: 0000-0001-5014-2486

Norbert Radacsi: 0000-0002-7358-951X

Notes

The authors declare no competing financial interest.

■ ACKNOWLEDGMENTS

This work is financial supported by the National Science Foundation of China (NSFC) (Grant nos. 61604025, 51728202), Chongqing Science and Technology Commission (Grant no. cstc2018jcyjAX0500), and Science and Technology Research Program of Chongqing Municipal Education Commission (Grant no. KJQN201800809).

■ REFERENCES

(1) Zhang, D.; Jiang, C.; Zhou, X. Fabrication of Pd-decorated TiO_2/MoS_2 ternary nanocomposite for enhanced benzene gas sensing performance at room temperature. *Talanta* **2018**, *182*, 324−332.

(2) Hirschmann, C. B.; Sinisalo, S.; Uotila, J.; Ojala, S.; Keiski, R. L. Trace gas detection of benzene, toluene, p-, m- and o-xylene with a compact measurement system using cantilever enhanced photoacoustic spectroscopy and optical parametric oscillator. *Vib. Spectrosc.* **2013**, *68*, 170−176.

(3) Xu, S.; Xu, Y.; Zhao, H.; Xu, R.; Lei, Y. Sensitive Gas-Sensing by Creating Adsorption Active Sites: Coating an SnO_2 Layer on Triangle Arrays. *ACS Appl. Mater. Interfaces* **2018**, *10*, 29092−29099.

(4) Ma, J.; Zhou, X.; Liu, L.; Zhu, Y.; Cheng, X.; Xu, P.; Li, X.; Deng, Y.; Zhao, D.; Ren, Y. Pt Nanoparticles Sensitized Ordered Mesoporous WO_3 Semiconductor: Gas Sensing Performance and Mechanism Study. *Adv. Funct. Mater.* **2018**, *28*, No. 1705268.

(5) Sun, X.; Hao, H.; Ji, H.; Li, X.; Cai, S.; Zheng, C. Nanocasting Synthesis of In_2O_3 with Appropriate Mesostructured Ordering and Enhanced Gas-Sensing Property. *ACS Appl. Mater. Interfaces* **2014**, *6*, 401−409.

(6) Kim, J.-W.; Porte, Y.; Ko, K. Y.; Kim, H.; Myoung, J.-M. Micropatternable Double-Faced ZnO Nanoflowers for Flexible Gas Sensor. *ACS Appl. Mater. Interfaces* **2017**, *9*, 32876−32886.

(7) Deng, S.; Tjoa, V.; Fan, H.; Tan, H.; Sayle, D. C.; Olivo, M.; Mhaisalkar, S.; Wei, J.; Sow, C. H. Reduced Graphene Oxide Conjugated Cu_2O Nanowire Mesocrystals for High-Performance NO_2 Gas Sensor. *J. Am. Chem. Soc.* **2012**, *134*, 4905−4917.

(8) Lee, J. H. Gas sensors using hierarchical and hollow oxide nanostructures: overview. *Sens. Actuators, B* **2009**, *140*, 319−336.

(9) Mirzaei, A.; Leonardi, S. G.; Neri, G. Detection of hazardous volatile organic compounds (VOCs) by metal oxide nanostructures-based gas sensors: a review. *Ceram. Int.* **2016**, *42*, 15119−15141.

(10) Zhang, J.; Qin, Z.; Zeng, D.; Xie, C. Metal-oxide-semiconductor based gas sensors: screening, preparation, and integration. *Phys. Chem. Chem. Phys.* **2017**, *19*, 6313−6329.

(11) Lu, G.; Ocola, L. E.; Chen, J. Reduced graphene oxide for room-temperature gas sensors. *Nanotechnology* **2009**, *20*, 445502−445509.

(12) Sun, J.; Bai, S.; Tian, Y.; Zhao, Y.; Han, N.; Luo, R.; Li, D.; Chen, A. Hybridization of $ZnSnO_3$ and rGO for improvement of formaldehyde sensing properties. *Sens. Actuators, B* **2018**, *257*, 29−36.

(13) Lee, H. Y.; Heish, Y. C.; Lee, C. T. High sensitivity detection of nitrogen oxide gas at room temperature using zinc oxide-reduced graphene oxide sensing membrane. *J. Alloys Compd.* **2019**, *773*, 950−954.

(14) Rong, X.; Chen, D.; Qu, G.; Li, T.; Zhang, R.; Sun, J. Effects of graphene on the microstructures of SnO_2@rGOnanocomposites and their formaldehyde-sensing performance. *Sens. Actuators. B* **2018**, *269*, 223−237.

(15) Pan, J.; Liu, W.; Quan, L.; Han, N.; Bai, S.; Luo, R.; Feng, Y.; Li, D.; Chen, A. Cu_2O and rGO Hybridizing for Enhancement of Low-Concentration NO_2 Sensing at Room Temperature. *Ind. Eng. Chem. Res.* **2018**, *57*, 10086−10094.

(16) Bhati, V. S.; Ranwa, S.; Rajamani, S.; Kumari, K.; Raliya, R.; Biswas, P.; Kumar, M. Improved Sensitivity with Low Limit of Detection of a Hydrogen Gas Sensor Based on rGO-Loaded Ni-Doped ZnO Nanostructures. *ACS Appl. Mater. Interfaces* **2018**, *10*, 11116−11124.

(17) Esfandiar, A.; Irajizad, A.; Akhavan, O.; Ghasemi, S.; Gholami, M. R. Pd WO_3/Reduced Graphene Oxide Hierarchical Nanostructures as Efficient Hydrogen Gas Sensors. *Int. J. Hydrogen Energy* **2014**, *39*, 8169−8179.

(18) Wang, Z.; Zhao, C.; Han, T.; Zhang, Y.; Liu, S.; Fei, T.; Lu, G.; Zhang, T. High-performance reduced graphene oxide-based room-

DOI: 10.1021/acsomega.9b00734
ACS Omega 2019, 4, 10252−10262

temperature NO_2 sensors: A combined surface modification of SnO_2 nanoparticles and nitrogen doping approach. *Sens. Actuators, B* **2017**, *242*, 269−279.
(19) Reddy, A.; Kokilab, M.; Nagabhushanac, H.; Sharmac, S.; Raod, J.; Shivakumarae, C.; Nagabhushanaf, B.; Chakradharg, R. Structural, EPR, photo and thermoluminescence properties of ZnO:Fe nanoparticles. *Mater. Chem. Phys.* **2012**, *133*, 876−883.
(20) Guo, W. Hollow and Porous $ZnSnO_3$ Gas Sensor for Ethanol Gas Detection. *J. Electrochem. Soc.* **2016**, *163*, B131−B139.
(21) Pei, S.; Cheng, H. The reduction of graphene oxide. *Carbon* **2012**, *50*, 3210−3228.
(22) Wang, Y.; Shao, Y.; Matson, D. W.; Li, J.; Lin, Y. Nitrogen-doped graphene and its application in electrochemical biosensing. *ACS Nano* **2010**, *4*, 1790−1798.
(23) Wang, J.; Ran, R.; Sunarso, J. K.; Yin, C.; Zou, H.; Feng, Y.; Li, X.; Zheng, X.; Yao, J. Nanocellulose-assisted low-temperature synthesis and supercapacitor performance of reduced graphene oxide aerogels. *J. Power Sources* **2017**, *347*, 259−269.
(24) Shi, J.; Cheng, Z.; Gao, L.; Zhang, Y.; Xu, J.; Zhao, H. Facile synthesis of reduced graphene oxide/hexagonal WO_3 nanosheets composites with enhanced H_2S sensing properties. *Sens. Actuators, B* **2016**, *230*, 736−745.
(25) Wang, H.; Robinson, J. T.; Li, X.; Dai, H. Solvothermal reduction of chemical lye foliated graphene sheets. *J. Am. Chem. Soc.* **2009**, *131*, 9910−9911.
(26) Wu, Z.; Zhou, G.; Yin, L.; Ren, W.; Li, F.; Cheng, H. Graphene/Metal Oxide Composite Electrode Materials for Energy Storage. *Nano Energy* **2012**, *1*, 107−131.
(27) Ghosh, S.; Adak, D.; Bhattacharyya, R.; Mukherjee, N. ZnO/γ-Fe_2O_3 Charge Transfer Interface toward Highly Selective H_2S Sensing at a Low Operating Temperature of 30 °C. *ACS Sens.* **2017**, *2*, 1831−1838.
(28) Zhao, X.; Li, Y.; Wang, J.; et al. Interactive oxidation-reduction reaction for the in situ synthesis of graphene-phenol formaldehyde composites with enhanced properties. *ACS Appl. Mater. Interfaces* **2014**, *6*, 4254−4263.
(29) Xia, Y.; Wang, J.; Xu, J.-L.; Li, X.; Xie, D.; Xiang, L.; Komarneni, S. Confined Formation of Ultrathin ZnO Nanorods/Reduced Graphene Oxide Mesoporous Nanocomposites for High-Performance Room-Temperature NO_2 Sensors. *ACS Appl. Mater. Interfaces* **2016**, *8*, 35454−35463.
(30) Jang, J.; Choi, S.; Kim, S.; Hakim, M.; Kim, I. Rational design of highly porous SnO_2 nanotubes functionalized with biomimetic nanocatalysts for direct observation of simulated diabetes. *Adv. Funct. Mater.* **2016**, *26*, 4740−4748.
(31) Richmond, H.; Myers, G.; Wright, G. The Reaction between Formaldehyde and Ammonia. *J. Am. Chem. Soc.* **1948**, *70*, 3659−3664.
(32) Fatmi, M. Q.; Hofer, T.; Rode, B. The stability of $[Zn(NH_3)_4]^{2+}$ in water: A quantum mechanical/molecular mechanical molecular dynamics study. *Phys. Chem. Chem. Phys.* **2010**, *12*, 9713−9718.
(33) Li, J.; Lu, Y.; Ye, Q.; Cinke, M.; Han, J.; Meyyappan, M. Carbon nanotube sensors for gas and organic vapor detection. *Nano Lett.* **2003**, *3*, 929−933.
(34) Guo, W. Design of Gas Sensor Based on Fe-Doped ZnO Nanosheet-Spheres for Low Concentration of Formaldehyde Detection. *J. Electrochem. Soc.* **2016**, *163*, B517−B525.
(35) Yang, H.; Wang, S.; Yang, Y. Zn-doped In_2O_3 nanostructures: preparation, structure and gas-sensing properties. *CrystEngComm* **2012**, *14*, 1135−1142.
(36) Bai, S.; Guo, J.; Shu, X.; Xiang, X.; Luo, R.; Li, D.; Chen, A.; Liu, C. Surface functionalization of Co_3O_4 hollow spheres with ZnO nanoparticles for modulating sensing properties of formaldehyde. *Sens. Actuators, B* **2017**, *245*, 359−368.
(37) Wang, S.; Cao, J.; Cui, W.; Fan, L.; Li, X.; Li, D. Constructing chinky zinc oxide hierarchical hexahedrons for highly sensitive formaldehyde gas detection. *J. Alloys Compd.* **2019**, *775*, 402−410.
(38) San, X.; Li, M.; Liu, D.; Wang, G.; Shen, Y.; Meng, D.; Meng, F. A facile onestep hydrothermal synthesis of NiO/ZnO heterojunction microflowers for the enhanced formaldehyde sensing properties. *J. Alloys Compd.* **2018**, *739*, 260−269.
(39) Chen, Z.; Hong, Y.; Lin, Z.; Liu, L.; Zhang, X. Enhanced formaldehyde gas sensing properties of ZnO nanosheets modified with graphene. *Electron. Mater. Lett.* **2017**, *13*, 270−276.
(40) Li, X.; Wang, J.; Xie, D.; Xu, J.; Dai, R.; Xiang, L.; Zhu, H.; Jiang, Y. Reduced graphene oxide/hierarchical flower-like zinc oxide hybrid films for room temperature formaldehyde detection. *Sens. Actuators, B* **2015**, *221*, 1290−1298.
(41) Han, M.; Liu, W.; Qu, Y.; Du, L.; Wei, H. Graphene oxide-SnO_2 nanocomposite: synthesis characterization, and enhanced gas sensing properties. *J. Mater. Sci. Mater. Electron.* **2017**, *28*, 16973−16980.
(42) Mishra, R.; Murali, G.; Kim, T.; Kim, J.; Lim, Y.; Kim, B.; Sahay, P.; Lee, S. Nanocube In_2O_3@RGO heterostructure based gas sensor for acetone and formaldehyde detection. *RSC Adv.* **2017**, *7*, 38714−38724.
(43) Sun, J.; Bai, S.; Tian, Y.; Zhao, Y.; Han, N.; Luo, R.; Li, D.; Chen, A. Hybridization of $ZnSnO_3$ and rGO for improvement of formaldehyde sensing properties. *Sens. Actuators, B* **2018**, *257*, 29−36.
(44) Zhao, Z.; Sun, Y.; Dong, F. Graphitic carbon nitride based nanocomposites: a review. *Nanoscale* **2015**, *7*, 15−37.
(45) Li, J.; Cushing, S. K.; Bright, J.; Meng, F.; Senty, T. R.; Zheng, P.; Bristow, A. D.; Wu, N. Ag@Cu_2O core-shell nanoparticles as visible-light plasmonic photocatalysts. *ACS Catal.* **2013**, *3*, 47−51.
(46) Wang, J.; Wang, Z.; Huang, B.; Ma, Y.; Liu, Y.; Qin, X.; Zhang, X.; Dai, Y. Oxygen Vacancy Induced Band-Gap Narrowing and Enhanced Visible Light Photocatalytic Activity of ZnO. *ACS Appl. Mater. Interfaces* **2012**, *4*, 4024−4030.
(47) Zhang, L.; Fang, Q.; Huang, Y.; Xu, K.; Chu, P. K.; Ma, F. Oxygen Vacancy Enhanced Gas-Sensing Performance of CeO_2/Graphene Heterostructure at Room Temperature. *Anal. Chem.* **2018**, *90*, 9821−9829.
(48) Wei, W.; Dai, Y.; Huang, B. Role of Cu Doping in SnO_2 Sensing Properties Toward H_2S. *J. Phys. Chem. C* **2011**, *115*, 18597−18602.
(49) Wang, J.; Chen, R.; Xiang, L.; Komarneni, S. Synthesis, properties and applications of ZnO nanomaterials with oxygen vacancies: A review. *Ceram. Int.* **2018**, *44*, 7357−7377.
(50) Zhou, D.; Kittilstved, K. Control over Fe^{3+} speciation in colloidal ZnO nanocrystals. *J. Mater. Chem. C* **2015**, *3*, 4352−4358.
(51) Shu, J.; Qiu, Z.; Lv, S.; Zhang, K.; Tang, D. Cu^{2+}-Doped SnO_2 Nanograin/Polypyrrole Nanospheres with Synergic Enhanced Properties for Ultrasensitive Room-Temperature H_2S Gas Sensing. *Anal. Chem.* **2017**, *89*, 11135−11142.
(52) Al-Enizi, A. M.; Naushad, M.; Al-Muhtaseb, A. H.; Ruksana; Alshehri, S. M.; Alothman, Z. A.; Ahamad, T. Synthesis and characterization of highly selective and sensitive Sn/SnO_2/N-doped carbon nanocomposite (Sn/SnO_2@NGC) for sensing toxic NH_3 gas. *Chem. Eng. J.* **2018**, *345*, 58−66.
(53) Abideen, Z. U.; Kim, J. H.; Mirzaei, A.; Kim, H. W.; Kim, S. S. Sensing behavior to ppm-level gases and synergistic sensing mechanism in metal functionalized rGO-loaded ZnO nanofibers. *Sens. Actuators, B* **2018**, *255*, 1884−1896.
(54) Liu, S.; Yu, B.; Zhang, H.; Fei, T.; Zhang, T. Enhancing NO_2 gas sensing performances at room temperature based on reduced graphene oxide-ZnO nanoparticles hybrids. *Sens. Actuators, B* **2014**, *202*, 272−278.
(55) Xia, Y.; Wang, J.; Xu, J.; Li, X.; Xie, D.; Xiang, L.; Komarneni, S. Confined Formation of Ultrathin ZnO Nanorods/Reduced Graphene Oxide Mesoporous Nanocomposites for High-Performance Room-Temperature NO_2 Sensors. *ACS Appl. Mater. Interfaces* **2016**, *8*, 35454−35463.
(56) Galstyan, V.; Comini, E.; Kholmanov, I.; Ponzoni, A.; Sberveglieri, V.; Poli, N.; Faglia, G.; Sberveglieri, G. A composite structure based on reduced graphene oxide and metal oxide

DOI: 10.1021/acsomega.9b00734
ACS Omega 2019, 4, 10252−10262

nanomaterials for chemical sensors. *Beilstein J. Nanotechnol.* **2016**, *7*, 1421−1427.
(57) Tai, H.; Yuan, Z.; Zheng, W.; Ye, Z.; Liu, C.; Du, X. ZnO Nanoparticles / Reduced Graphene Oxide Bilayer Thin Films for Improved NH_3-Sensing Performances at Room Temperature. *Nanoscale Res. Lett.* **2016**, *11*, 130.
(58) Van Quang, V.; Dung, N. V.; Trong, N. S.; Hoa, N. D.; Duy, N. V.; Hieu, N. V. Outstanding Gas-Sensing Performance of Graphene/SnO_2 Nanowire Schottky Junctions. *Appl. Phys. Lett.* **2014**, *105*, No. 013107.

DOI: 10.1021/acsomega.9b00734
ACS Omega 2019, 4, 10252−10262